High speed visualizations of the cavitating vortices of 2D mixing layer

V. Aeschlimann [a], S. Prothin [b], S. Barre [a], H. Djeridi [c,*]

[a] LEGI UMR 5519, Domaine Universitaire BP53, 38041, Grenoble Cedex 9, France
[b] Institut de Recherche de l'Ecole Navale (IRENav, EA3634), Ecole Navale BP 600, 29240, BREST ARMEE, France
[c] Laboratoire de Physique des Océans, UMR 6523, Université de Bretagne Occidentale (UBO), 6 Av Le Gorgeu, BP 809, 29285 Brest Cedex, France

ARTICLE INFO

Keywords:
Turbulent mixing layer
Cavitation
Image analysis
Vortex dynamics

ABSTRACT

The present study investigates experimentally vortex dynamics of a cavitating two-dimensional mixing layer at a high Reynolds number in order to determine the effect of growth and collapse of cavitation. The dynamics and the topology of the vorticity regions corresponding to the low pressure area where cavitation effects take place are studied from the single phase state to highly cavitating conditions. LDV techniques are used in order to characterize the pattern of the turbulent single phase flow. High-speed visualizations have been performed using a specific image processing of time series to highlight the behaviour and dynamics of the vapour phase. Visualizations, image processing and statistical analysis enable the estimation of the convective velocity and the shedding frequency of the cavitating Kelvin–Helmholtz vortices. The measured visual vapour thickness grows linearly as the Kelvin–Helmholtz instability develops and its expansion rate stays constant for the range of cavitation levels studied. The vortex pairing phenomenon is also analysed. Results show that the spatial development of the mixing area is slightly affected by the vapour phase allowing a self-similar behaviour of the mean motion.

1. Introduction

Cavitation occurs in liquid flows when the local pressure reaches values lower than the vapour pressure, inducing vaporization. This phenomenon causes some potentially negative effects such as performance deterioration, vibrations, noise and cavitation erosion. Furthermore, cavitating structures exhibit various shapes and behaviours such as stable or pulsating sheet cavities, shedding vapour clouds or diphasic vortices where the liquid is sheared. The global context of the present study is an investigation of the cavitating flows in the rocket engine turbopump inducers. In order to predict this type of complex two-phase flow, the present study focuses on a cavitating plane mixing layer to provide a better understanding of the cavitation–turbulence relationship.

A brief overview of the bibliography shows that an effort has been devoted to characterize the vapour repartition on the blades of the real inducer geometry [1,2], but the turbulence properties and the dynamics of the cavitating structures could not be characterized due to the technical difficulty of performing measurements on a rotating device with a highly complex geometry. Two-dimensional geometries (venturi geometries) have been tested to reproduce on their wall the pressure field existing on the suction side of an inducer's blade. An attached cavitating sheet at the wall was observed in a flow separation. The dynamics of the vapour structure were defined for two different cases, a steady cavitation sheet and a pulsating one shedding diphasic vortices. Velocity measurements highlighted the re-entrant jet dynamic [3–7]. Simultaneously, numerical simulations have been also devoted to reproducing the shape and the dynamics of the cavitating structures, but the lack of local experimental data prevented from justifying numerical hypotheses such as the turbulent viscosity [8]. This is the reason why the choice of a fundamental case, in order to limit flow complexity, is crucial to quantify parameters affecting the cavitating development and the turbulent topology of the flow. This point of view has led us to study a two-dimensional mixing layer where no recirculating area was present and no wall interaction occurred. Similar two-dimensional cavitating sheared flows have been studied by O'Hern [9] and Iyer and Ceccio [10] where the maximum average void ratio observed was about 1% and no spatial nor temporal quantitative analysis of the vapour distribution were performed. However, the mixing layer flow is sufficiently representative of the inducer blade cavitation sheet, particularly when focusing to the rear sheet zone where a re-entrant jet occurs [6]. This reference test provides a well-documented test case to be used to quantify the turbulence–cavitation interactions and therefore the dynamics of the cavitating structures.

In previous works O'Hern [9] studied the cavitating mixing layer developing on a sharp-edged plate and focused on the inception of cavitation inside the mixing area with large physical dimensions

* Corresponding author. Tel.: +33 4 76 82 70 27; fax: +33 4 76 82 52 71.
E-mail address: henda.djeridi@legi.grenoble-inp.fr (H. Djeridi).

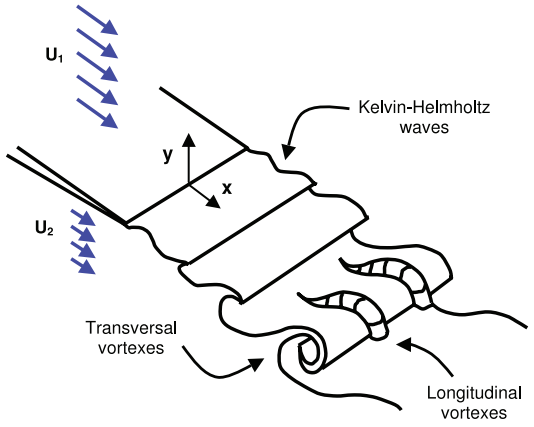

Fig. 1. Scheme of Kelvin–Helmholtz instabilities.

Fig. 2. Instantaneous picture of the cavitating shear layer (Weinberger SpeedCam Visario—shutter time 20 μs).

allowing a detailed optical flow diagnostics. They put in evidence the importance of the streamwise vortices in the cavitation inception process as the key to explain the commonly observed Reynolds dependence of the inception index. More recently, Iyer and Ceccio [10] studied the influence of developed cavitation on the flow of a turbulent shear layer using P.I.V.–L.I.F. techniques (Particle Image Velocimetry–Laser Induced Fluorescence). Their visual observations of the shear layer suggested that the overall formation, growth and convection of the primary and secondary vortical structures are not significantly affected by the presence of the vapour phase and the largest differences between cavitation and non-cavitating case in the centre of the shear layer consisted in the increase of turbulent fluctuations by about 15%. Bubble growths and collapses increased the turbulence levels, as expected by Laberteaux and Ceccio [11].

Taking into account these results, one of the aims of the current research was to characterize the vapour phase dynamics of a two-phase mixing layer through high resolution visualizations with specific signal processing for higher averaged void ratios (about 17% measured by Aeschlimann et al. [12], for the present studied flow compared to 1.5% for the Iyer and Ceccio [10] study). In fact, the present plane mixing layer was formed by two streams of water moving at different velocities initially separated by a splitter plate. Kelvin–Helmholtz instabilities developed at the interface and became eddies along the longitudinal direction (see Fig. 1).

These vortices are characterized by a specific convective velocity and shedding frequency, vortex-pairing phenomenon, and mixing layer expansion rate [13]. Concerning the cavitating shear layer, the vapour appears in the vortex core where the pressure is lower than outside the mixing area. When the pressure decreases, the Kelvin–Helmholtz vortices become clearly identified by visualizations (see Fig. 2) where the vapour is white and the liquid is dark.

Time resolved movies enable us to analyse the two-phase large scale structure dynamics as demonstrated by Brown and Roshko [14], in the case of the analysis of spark shadow pictures, concerning the density effects in turbulent mixing layers. Statistical analyses of the visualization are also used for growth rate determination of the mixing area as presented in Papamoschou and Roshko's [15] study, where Schlieren photographs were used in the case of compressible turbulent shear layer. Concerning the cavitation behaviour, many examples of visualization and observation have been performed. Can be mentioned the detailed action of travelling bubble near the solid boundary studied using visualizations by Ceccio and Brennen [16], or the Laberteaux et al. [17] observations of cavitating vortices in the closure region of a partial attached cavity by using a super-high-speed camera. More recently, Saito and Sato [18,19] implemented a refined visualization and analysis method by using high-speed video camera triggered by an impulsive acceleration pulse to put in evidence the collapse behaviour of cloud cavitation in a convergent–divergent nozzle.

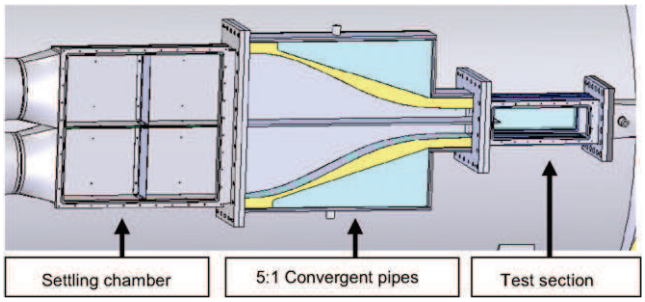

Fig. 3. Sketch of the experimental set-up.

In this context, using high-speed visualizations, the present study implemented a specific image processing based on the grey level transversal profiles of the frames and a spatio-temporal correlation method in order to highlight the dynamics of the large scale structures of the mixing layer. The originality of the present work consists in the systematic comparison with the single-phase flow characteristics in order to highlight the cavitation–turbulence interactions. The paper is organized as follows: Section 2 briefly presents the experimental set-up and flow configurations and the image processing tools, while Section 3 is devoted to a description of the topology of the flow using different approaches, whereas the final discussion concluding the paper is presented in Section 4.

2. Experimental apparatus and flow configurations

2.1. Test facilities

Experiments were conducted in CREMHyG, hydraulic research centre of Grenoble, in a shear layer test bed. The rectangular test section was 300 mm long and had a cross-section that expands from 80 by 80 mm at the inlet to 80 by 88.8 mm at the outlet. The studied shear layer was 2D, the inlet section was divided in two halves. The splitting plate was 6 mm thick and ends by a rounded edge of 0.4 mm diameter. Liquid water was used as the test fluid for this experiment. The test bed was set in a hydraulic closed-circuit including a regulated water pump and a free surface tank. Downstream of the water pump the flow was divided in two separated flows, a high speed one and a low speed one. Then both flows crossed a settling chamber containing honeycomb frames and grids in order to homogenize the flow and to break large scale structures. Further on, flows were accelerated in a 5:1 convergent pipes: boundary layers were reduced to restrict the wake effect at the splitting plate tip. Based on the method described in [20], convergent profiles have been optimized to avoid flow separation and cavitation at the wall. Fig. 3 shows a sketch of this experimental set-up.

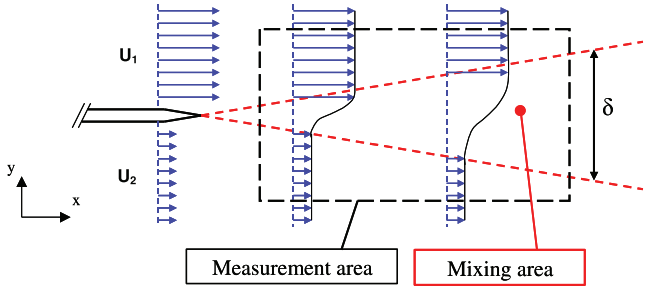

Fig. 4. Schematic representation of the mixing layer.

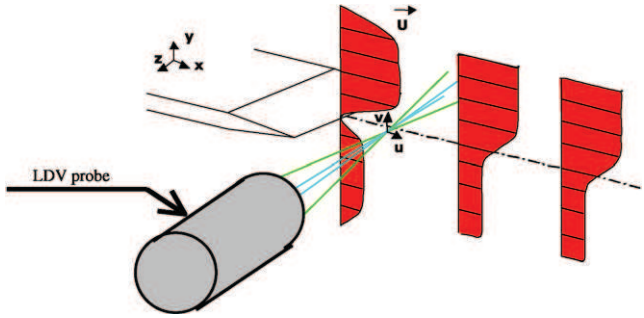

Fig. 5. Sketch of the LDV set-up.

In this configuration the studied case is a traditional mixing layer, where the inlet conditions are $U_1 = 15.8$ m/s for the high-speed side and $U_2 = 3.5$ m/s for the low speed side (see Fig. 4). The tip of the splitter plate is located at $x = 0$ mm and $y = 0$ mm.

The conditions for cavitation were controlled by the difference between a pressure reference located in the inlet section and the vapour pressure of the fluid. The operating point was characterized by the reference cavitation number σ defined in the inlet reference section:

$$\sigma = \frac{P_2 - P_v}{0.5 \cdot \rho \cdot (U_1 - U_2)^2}. \quad (1)$$

P_2 is the averaged pressure measured at the wall in the inlet section of the low speed flow. P_v is the vapour pressure which depends on the water temperature. The cavitation numbers used were $\sigma = 0.167$ and 0.102 (corresponding to a weak cavitation level called respectively *cav*1 and *cav*2) and $\sigma = 0.012$ (corresponding to the well developed cavitating Kelvin–Helmholtz vortices, called *cav*3). The inception operating point was also studied, it was estimated at $\sigma = 0.208$ where cavitating structures start to appear (*cav*0). Water temperature measurement was required to calculate the vapour pressure and to set the selected cavitation number. The recorded water temperature varied within the range of 10 °C–25 °C depending on operating and atmospheric conditions. All operating points have been fixed by the upstream pressure using an absolute pressure sensor (Druck PMP 4070) with an uncertainty of about 19 Pa and the sigma value was given with a precision of 0.007 for $\sigma = 0.208$ (corresponding to *cav*0) and 0.001 for $\sigma = 0.012$ (corresponding to *cav*3) taking into account the regulation system, precision of the pressure sensor and the density value of the water with temperature. Taking into account that dissolved gas concentration inside the water plays a major role in cavitation inception [21], the main objective was to obtain a reproducible cavitating conditions. To achieve reproducible experiments, a degasification protocol was established during 1 h for each condition and the dissolved O_2 concentration has been measured (acquired with an Orbisphere MOCA O2 probe) at the beginning and during all experiments. The level of dissolved air is constant, fixed at 3.5 *ppm*, for each test condition and the sensor precision was ±1%. After 1 h, the *rms* value of the concentration was about 8.29×10^{-3} and the relative deviation of 0.25%.

2.2. Mixing layer configuration in non-cavitating case

To characterize the structure of the single phase mixing layer, detailed velocity measurements have been performed using Laser Doppler Velocimetry technique (LDV). A two-component four-beam LDV Dantec Dynamics system was used to measure velocities in water seeded with 10 μm silver plated glass spheres. The system was operated in backward scattering mode and was coupled with two enhanced burst spectrum analysers (BSA). The spatial dimension of the probe volume (LDV) in vertical and longitudinal directions is 0.115 and 2.4 mm in the transversal direction (z). The optical probe was located as sketched in Fig. 5.

The time histories were recorded with 20,000 samples acquired in about 4 s. This parameter corresponds to a mean data rate of 5 kHz which is sufficient to obtain the mean and *rms* value with an uncertainty estimated with statistical consideration to be roughly 2%. A spectral analysis of the longitudinal velocity signal has been conducted with a spectral resolution of 2 Hz. This spectral analysis was provided by the Fast Fourier Transform method after re-sampling the signals with a constant data rate.

2.3. Flow visualizations and image processing

To quantify the dynamics of the cavitating mixing layer, flow visualizations have been performed using high-speed camera and a specific image processing has been applied to characterize the two-phase flow mixing, vortex convection and typical vortex frequency.

2.3.1. Visualization set up

The flow visualization was performed using a SpeedCam Visario Weinberger (high speed camera) operated with a 2 kHz frame rate. The full resolution is 1024 ∗ 768 pixels. The lens used has a 50 mm focal length in the standard configuration. The light source is composed of two continuous spots used with a diffusion device. The processed images have a dimension of 1024 ∗ 352 pixels. The number of images recorded by film is 8192, which corresponds to an observation time of 4.096 s. This is a sufficient time to take into account the well-known spatio-temporal scale of single phase mixing layer. The shutter time of 20 μs was small enough to freeze the flow and consider each picture instantaneous. The scale factor is 0.279 mm/pixels. Grey levels were reversed compared to original images. An example of such images is shown in Fig. 6 where the different regions of the flow are visualized for the developed cavitation case corresponding to $\sigma = 0.012$.

Because the kernels of the coherent structures are governed by low pressure, the Kelvin–Helmholtz instability is clearly shown. The cavitating vortices are visualized by white regions and the non-cavitating regions are black. Flow is from the left to right with the upper layer having the higher velocity. The vortical structures, which characterized the Kelvin–Helmholtz instability, extend along the entire test section (along x-axis). It can be seen that neighbouring pairs of vortices roll around each other in the mixing layer leading to a vortex-pairing phenomenon (see sketches in Fig. 6). All the structures remains aligned across the stream and appear two-dimensional.

2.3.2. Image processing

Image processing is based on the temporal fluctuations of the greyscale signal. The function, called $G_S(t)$, is taken in the (x, y) plane of the mixing layer and can be defined for each pixel of the processed image : $G_S(x, y, t)$. Before extracting signal, statistical

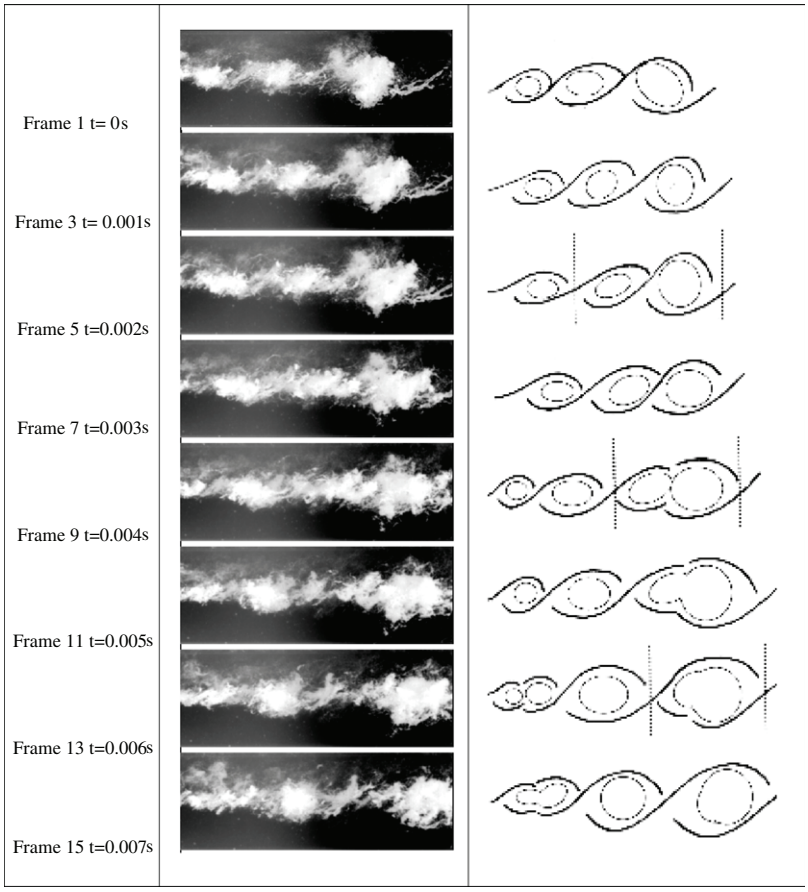

Fig. 6. Section views of Kelvin–Helmholtz vortices ($cav3, \sigma = 0.012$).

study has been made allowing characterizing the mean vapour expansion rate of the cavitating mixing layer. Averaging 8192 pictures, it was possible to obtain a (x, y) map for the mean value $\overline{G_S}$:

$$\overline{G_S(x,y)} = \frac{\sum_{t=1}^{8192} G_S(x,y,t)}{8192}. \tag{2}$$

Cavitating mixing layer appears within a cone with an aperture equal to the vapour thickness expansion rate ($\delta'_v = \mathrm{d}\delta_v/\mathrm{d}x$). In order to determine, for each x position, the vapour thickness δ_v of the cavitating mixing layer, a boundary determination algorithm was used.

It is clear that it is quite easy to observe the Kelvin–Helmholtz dynamics on $G_S(x, y, t)$ signal. Vapour structures appear regularly and are separated by low G_S events corresponding to the inter-eddy space. Both a convection velocity for large scale vapour structures and a Strouhal number can be defined by processing such data. In order to compute statistical characteristics, the fluctuating signal for each location is normalized to obtain a dimensionless grey level fluctuation as:

$$S(t) = \frac{G_s(t) - \overline{G_s}}{\sqrt{\overline{G_s'^2}}} \tag{3}$$

where $\overline{G_s}$ is the mean value of the G_s signal over the considered observation time and $\overline{G_s'^2}$ is its variance. $S(t)$ has been used to calculate the convective velocity U_C of the coherent structures of the cavitating mixing layer. This velocity was calculated by using the cross spectrum of two signals taken at two different x positions. The distance between these two points is dx measured in the x direction. For separate time series $S_1(t)$ and $S_2(t)$ the cross-spectrum is defined by:

$$I_{s_1 s_2}(f) = S_1(f) \bullet S_2^*(f) \tag{4}$$

where $S_1(f)$ is the spectrum of $S_1(t)$ and $S_2 * (f)$ the conjugate. The real part of the cross spectrum (co-spectrum $Co(f)$) and the imaginary part (quadra-spectrum $Qu(f)$) are used to calculate the phase between the two signals by:

$$\varphi(f) = arctg\frac{Qu(f)}{Co(f)}. \tag{5}$$

A consistent and optimal cross spectrum is given by an optimization of dx parameter corresponding to the best cross-correlations, in the middle of the mixing layer (associated with cavitating vortex sizes). Using optimal value of dx, the convection velocity U_C is given by:

$$\varphi_0 = 2\pi \cdot F_0 \cdot \frac{\mathrm{d}x}{U_C} \tag{6}$$

where F_0 is the shedding frequency of Kelvin–Helmholtz instability corresponding to the co-spectrum maximum frequency.

To qualitatively estimate the behaviour of KH vortices, average grey level is computed in vertical direction of each image and grey level profile and contour map can be extracted. Saito and Sato [19] used this technique in order to estimate the mechanism of unsteady behaviour of cloud cavitation in the case of convergent–divergent nozzle. The results of this time series analysis of average grey level versus a longitudinal direction for different cavitation cases represent the ratio between time and location and then the slope gives an estimation of the individual convection velocity of the cavitating structure. This method has been compared to the cross-correlation method.

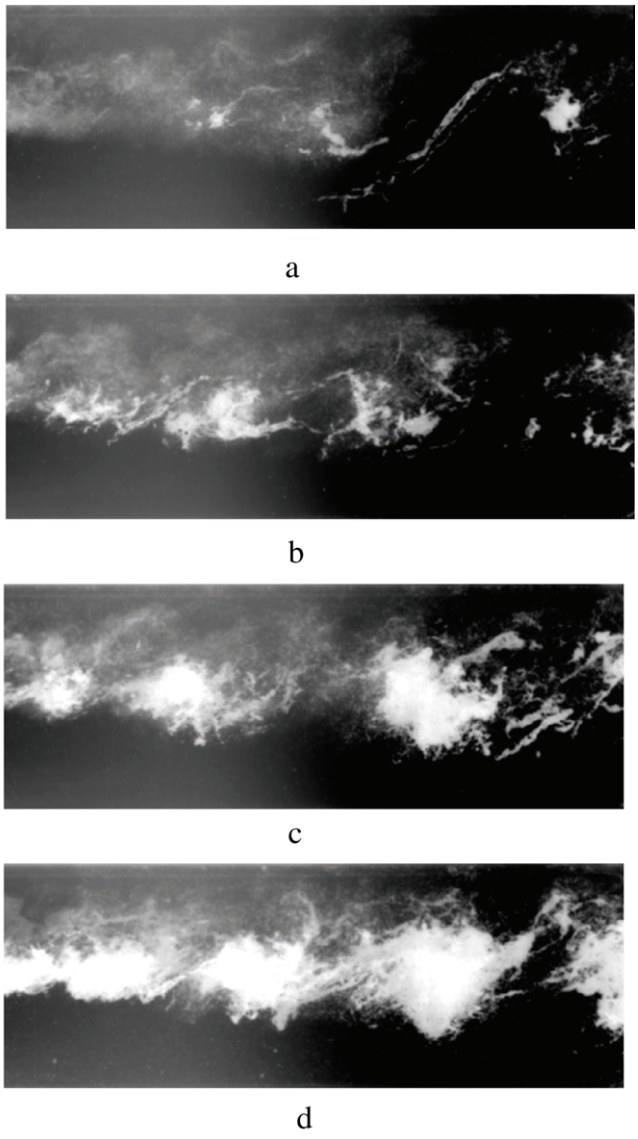

Fig. 7. Visualization of cavitating mixing layer; (a) $cav0$; (b) $cav1$; (c) $cav2$; (d) $cav3$.

3. Topology of the cavitating mixing layer

3.1. Growth rate evolution

From the $cav0$ case, image exhibits inception of cavitation where the secondary vortices (vortex tube like "spaghetti") are primary visualized. When the pressure is decreased, until $cav3$ case, the Kelvin–Helmholtz vortices are clearly visualized (Fig. 7).

With the aim to characterize the vapour thickness δ_V, the averaged image of each acquired set was analysed. Firstly, in order to correct the heterogeneous light dispersion over the measurement area, a background picture was captured without cavitating structure. Then, this background reference was subtracted from the averaged picture of each set. From these corrected average pictures, transversal grey level profiles were extracted and analysed; see for example Fig. 8. Grey level profiles had symmetrical shapes around the mixing area centre; $y = 0$ mm, where the maximum greyscale value was observed. From the centre, greyscale value decreased on both sides until it stabilized to a constant value corresponding to the liquid water flows. A vapour thickness, δ_v, was defined corresponding to the area where the greyscale was greater than a threshold of 1.3 times the value

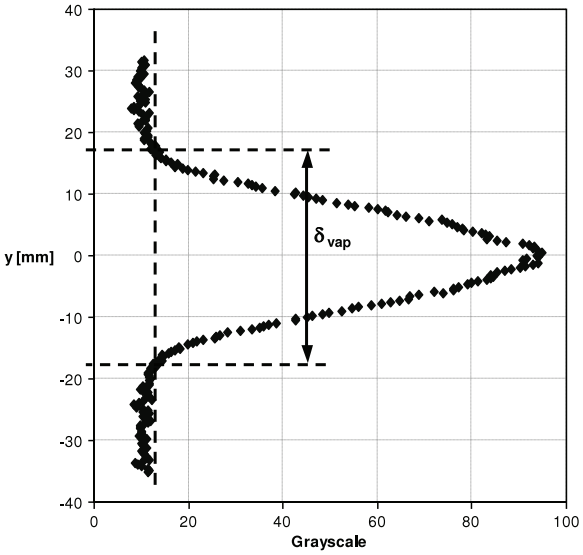

Fig. 8. Example of an extracted grey mean level profile ($cav2$; $x = 112$ mm).

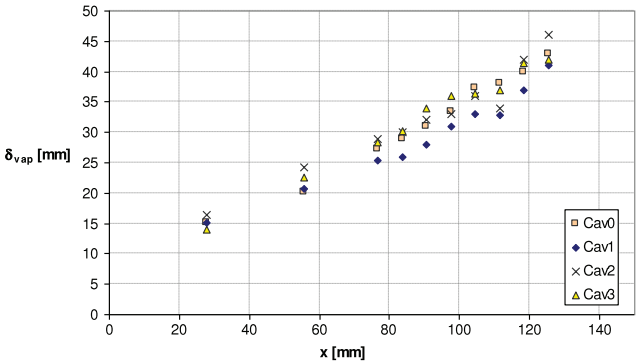

Fig. 9. Vapour thickness longitudinal evolution.

outside the mixing area where only pure liquid water was present (see Fig. 8). This threshold was chosen as small as possible but sufficient to not detect variation due to noise on the profiles. The growth of the shear layer is displayed Fig. 9 for different cavitation levels.

Then, Fig. 9 exhibits the vapour phase thickness longitudinal evolution for the different test cases. It is clear that no major change in the vapour thickness evolution can be observed due to cavitation effects.

It seems clear that the vapour is generated in the Kelvin–Helmholtz vortices cores where the mean velocity shear is maximal. Due to this shear, a transverse pressure gradient between the shear layer core and its boundaries is created. The vapour affected zone is then growing from the layer core towards its boundaries when σ decreases. This leads to a slight increase of δ_V with the developed cavitation. Nevertheless, the main result consists in a quasi-linear longitudinal evolution of the vapour thickness; so that the selfsimilarity is preserved when cavitation number decreases inducing a similar development of Kelvin–Helmholtz eddies as expected in single phase flow. This visual thickness can be confronted to the vorticity thickness δ_ω characteristic of the development of Kelvin–Helmholtz instabilities at the interface of the layers in both the single and two-phase mixing layer cases. Aeschlimann et al. [12,22] defined this quantity from the velocity profiles and observed the same self-preserved area of the mixing layer. In the present study the estimated value $\delta_v \approx 2\delta_\omega$ is obtained. We also note that the vorticity thickness expansion rate is

roughly unchanged by the cavitation process. This fact may be explained by the relatively low void fraction observed in the studied flow. Indeed, the vapour itself transports very little momentum because of its very low density. Therefore it can be conjectured that the vapour effect on the mean velocity fields remains negligible in the void ratio range covered by the present study as shown in [22].

3.2. Observations of the large eddy behaviour

(a) *convective velocity*. Firstly, to estimate the behaviour of the cavitating vortices, average grey level transversal profiles are extracted on each image and plotted versus longitudinal direction:

$$E_1(x,t) = \frac{\int_{-\delta_V/2}^{\delta_V/2} G_S(x,y,t)\mathrm{d}y}{\delta_V}. \tag{7}$$

The average grey levels characterize the passage of cavitating structures and for each time depending image, higher grey levels correspond to the coherent structure localization. This leads to a shedding process topology and a spatio-temporal description of the vortices behaviour (see Fig. 10(a) for $cav2$ case). Then, by repeating this process in time for each acquired image, we may obtain a contour map of stripes (see Fig. 10(b) for $cav2$ case). Typical spatio-temporal diagrams are then obtained. On such diagrams, the Kelvin–Helmholtz instabilities corresponding to vertical structures are visible as the oblique stripes. Near the splitter plate, the wake area is characterized by small dispersed stripes. In the self-similar area (from $x = 80$ mm, see [22]), large scale structures are identified by the wave-like structures. This enables a determination of the convective velocity of the transient vortices. It can be seen from the contour map of the spatio-temporal diagram that the coloured regions from green to red indicate the cavitating zones. Pairs of oblique stripes appear in addition to single stripes corresponding to the vortex pairing.

In order to track each structure individually on the spatio-temporal diagram, a peak detection algorithm is performed. Firstly, a smoothed diagram is obtained to reduce noises so only one maximum per stripes remains. The smoothed profiles are defined from a space–time moving average:

$$E_2(x,t) = \frac{\int_{x-\Delta x}^{x+\Delta x}\int_{t-\Delta t}^{t+\Delta t} E_1(x,t)\,\mathrm{d}x\,\mathrm{d}t}{\Delta x\,\Delta t} \tag{8}$$

where $\Delta x = 4.2$ mm and $\Delta t = 2.5$ ms.

A threshold is then applied to filter the small structures and main KH structures are tracked by detecting the maximums of $E_2(x,t)$ (Fig. 10(a) and (c)).

The previously described method has been applied to each cavitating cases (from $cav1$ to $cav3$) in order to determine the convective velocity of large scale structures. Results are abstracted in Fig. 11 where the detection of the stripes peak values is showed for the three studied cases (only 250 ms observation time to ease the structure identification). Noisy stripes are identified in the $cav1$ case which result from the intermittent inception of cavitation when the pressure is high. Starting with an unstable behaviour near the splitter plate, we observe vortical structures convected at the speed $\mathrm{d}x/\mathrm{d}t$ ranging from 9 to 11 m/s which falls within the range of the theoretical value of the convective velocity $U_C = 8$–9 m/s at $x = 100$ mm for the three tested cavitation cases. From these results, it appears that the vortices convective velocity seems almost unaffected by the cavitation level and that little dispersion in the phase velocity is observed for such vortices. Thus vapour is carried within the Kelvin–Helmholtz vortices.

The convective velocity of the Kelvin–Helmholtz vortices can also be deduced by using formula (6) with the optimal $\mathrm{d}x$ corresponding to the maximum cross-correlation function at each studied point. The Kelvin–Helmholtz shedding frequency F_0 and the

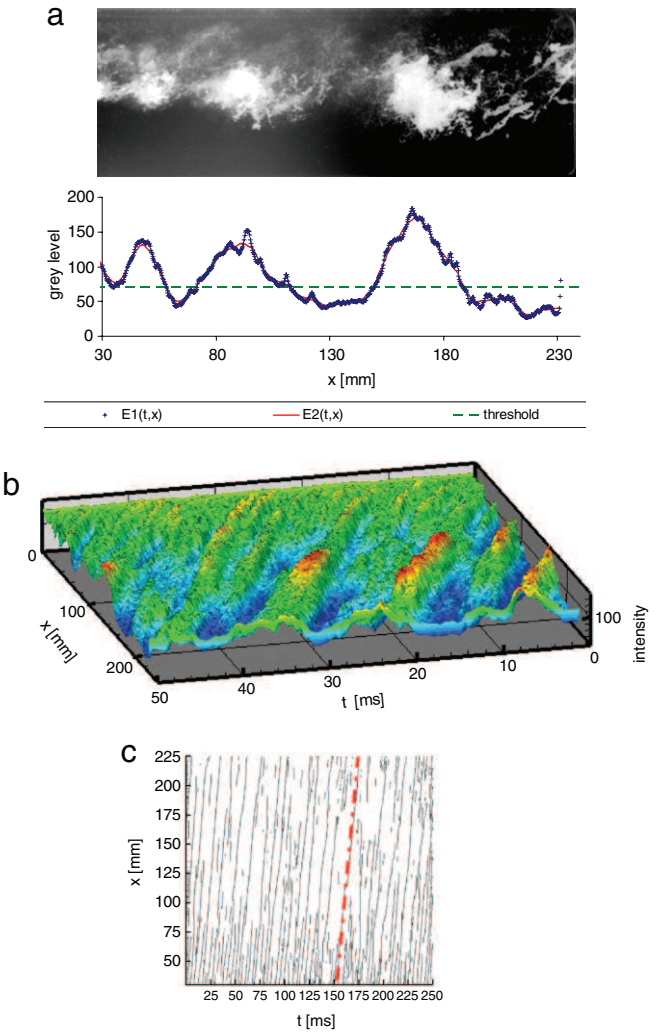

Fig. 10. Spatio-temporal diagram; (a) spatial average grey level, (b) contour map of stripes, (c) detection of peak values of stripes ($cav2$).

phase φ_0 are determined from the cross-spectrum analysis. Fig. 12 presents an example of the amplitude and phase of the cross-spectrum between two signals at $x = 120$ mm, $y = 0$ mm and $\sigma = 0.012$ where $\mathrm{d}x = 15.6$ mm and $\delta_\omega = 16.2$ mm [22]. It can be seen that the amplitude of this cross-spectrum ($Co(f)$) mainly contributes to the correlation at rather low frequencies, leading to a maximum contribution near $F_0 = 100$ Hz. This frequency corresponds to the most energetic cross-contribution and has the same order of magnitude as the frequency obtained in the non-cavitating mixing layer. The phase is positive and increases until $f = 400$ Hz. Beyond this value, phase distribution is mainly flat over quite a wide range of frequencies with some oscillations for the highest frequencies for which spectral coherency becomes very low. The same trend is observed at different positions in the mixing layer.

Fig. 13 presents the longitudinal evolution (along the x-axis) of the convective velocity U_C of the Kelvin–Helmholtz vortices as determined with formula (6) from the cross-spectra maximum energy and phase (see Fig. 12). These results correspond to data obtained for $y = 0$ mm which is the middle of the mixing layer and for three different cavitation levels ($\sigma = 0.012$; 0.102 and 0.167) and this velocity is normalized by the theoretical value:

$$U_{C\mathrm{th}} = \frac{U_1 + U_2}{2} \tag{9}$$

obtained by Aeschlimann et al. [22] in two-phase flow using PIV–LIF. The convective velocity evolution is presented with error

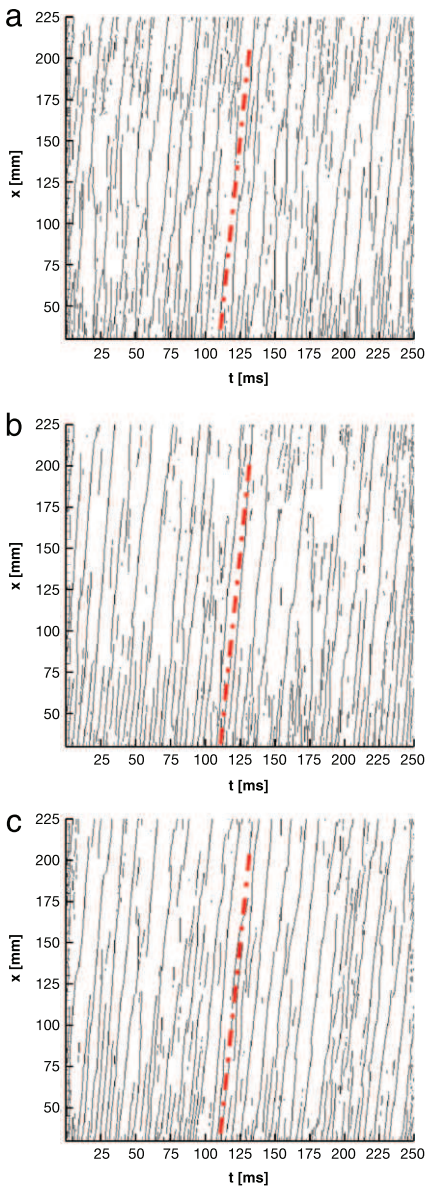

Fig. 11. Spatio-temporal diagram for the three cases of cavitation (the dashed line represents the slop for the determination of convective velocity). (a) $cav1$; (b) $cav2$; (c) $cav3$.

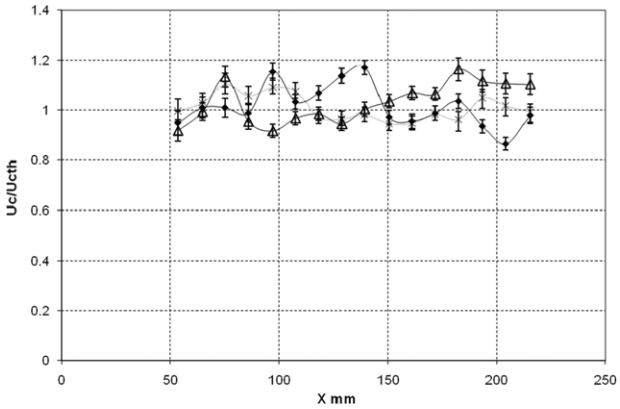

Fig. 13. Longitudinal evolution of the normalized convective velocity for ♦: $\sigma = 0.167$ ($cav1$), ×: $\sigma = 0.102$ ($cav2$), △: $\sigma = 0.012$ ($cav3$).

bars corresponding to uncertainties due to the cross-spectral resolution of about $\Delta f = 0.97$ Hz and spatial resolution of the high speed camera $\Delta(\mathrm{d}x) = 0.279$ mm. The maximum value of uncertainties is almost 5% for the convective velocity estimation.

From Fig. 13 it is clear that no longitudinal trend can be observed for the three studied flows. It also can be noticed that the longitudinal average of this data leads to an almost constant value for the large eddy convection velocity when changing cavitation level. It can also be concluded that the estimation of the convective velocity using the cross-correlation method between two signals extracted from the high speed visualization is in a good agreement with the theoretical value locally measured in the mixing layer.

These precise results, from correlation method, corroborate those obtained by the slope estimation on spatio-temporal diagrams.

(b) *coherence of the cavitating KH vortices*. The vortex coherence is given by:

$$Coh(f) = \frac{Co^2(f) + Qua^2(f)}{S_1(f)\, S_2(f)}, \tag{10}$$

and its evolution versus frequency is shown in Fig. 14 for two locations in the mixing layer. For the cavitating cases studied, the Kelvin–Helmholtz vortices exhibit a high level of coherence for a frequency range around 100–200 Hz. For this frequency domain, we observe values over 80% for the vortices coherence function. Above 400 Hz, the coherence exhibits a slight decrease until around a value of 0.1. However, beyond $f = 400$ Hz, the signal power density is quite low and it can then be concluded that most of the energetic eddies (for $f < 400$ Hz) exhibit a very high coherence level.

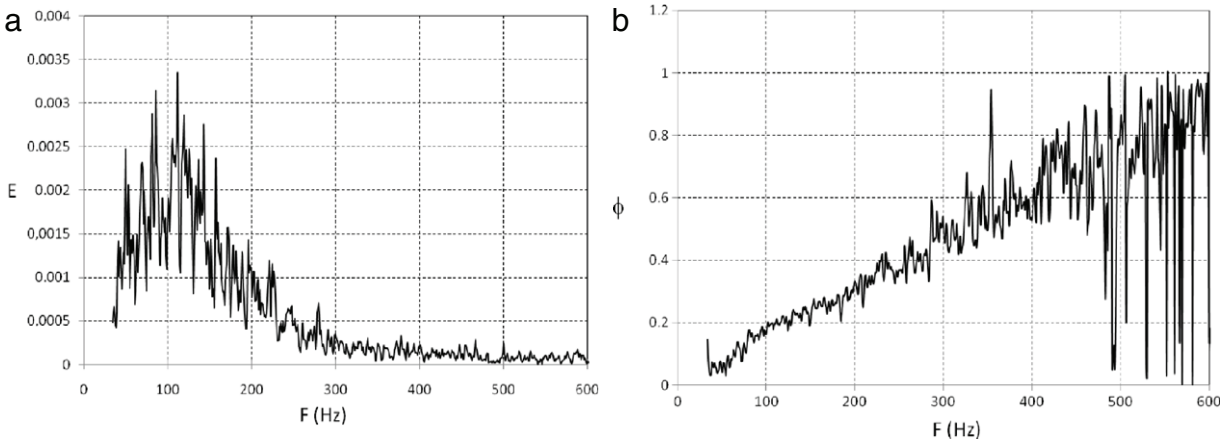

Fig. 12. Example of $Co(f)$ (a) and phase (b) between two signals for $x = 120$ mm, $y = 0$ mm and $\sigma = 0.012$ ($cav3$).

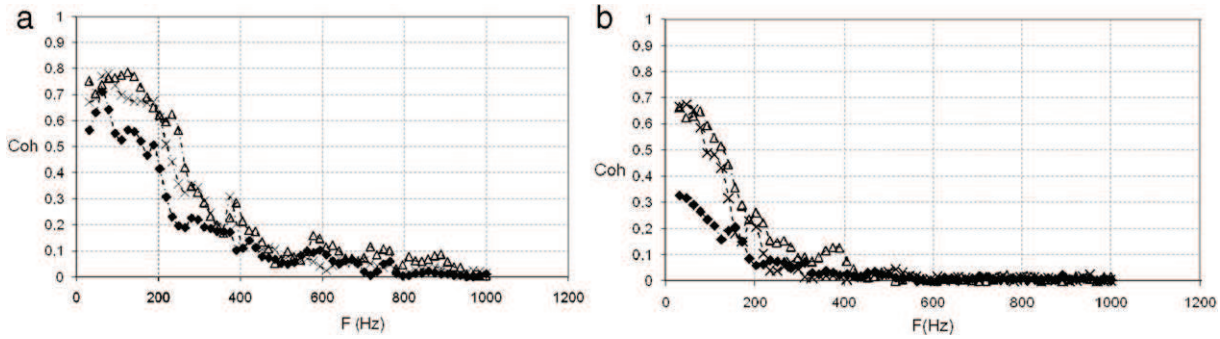

Fig. 14. Coherence function at $x = 120$ mm (left), and $x = 215$ mm (right). ♦: $\sigma = 0.167$ ($cav1$), ×: $\sigma = 0.102$ ($cav2$), △: $\sigma = 0.012$ ($cav3$).

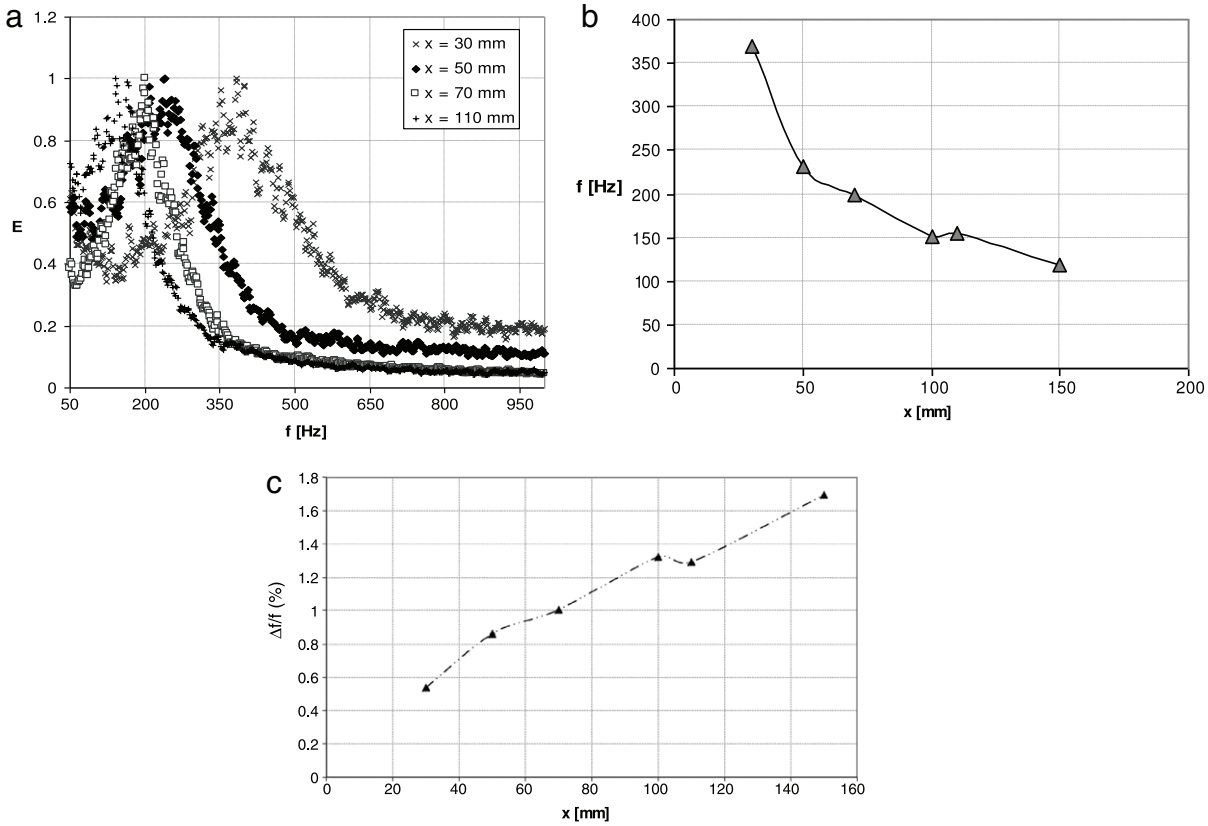

Fig. 15. (a) Longitudinal velocity spectra, (b) maxima of the peak frequency evolution for several positions in the non-cavitating mixing layer, (c) relative error of the peak frequency evolution.

Detailed observations indicate that for $x = 120$ mm the maximum of coherence is obtained for the high level of cavitation and the frequency range 100–200 Hz is predominant. When the pressure in the mixing layer is increased, a loss of coherence can be observed, in particular from 200 Hz. A similar trend is observed for $x = 215$ mm where the loss of coherence is globally pointed out.

3.3. Shedding process and Strouhal frequency

In order to evaluate the effect of cavitation on the Kelvin–Helmholtz vortices, the Strouhal frequency can be compared with that obtained by LDV in the non-cavitating mixing layer. Longitudinal velocity spectra were then obtained using the method described in Section 2.2 of the present paper. Fig. 15(a) shows some examples of these spectra for $y \approx \delta_v/2$ at several longitudinal position ranging from $x = 30$ mm to $x = 150$ mm. Some peaks are clearly observable showing that the peak frequency (displayed on Fig. 15(b)) changes with respect to the considered longitudinal position. The spectral analysis has been performed with a spectral resolution of $\Delta f = 2$ Hz and the relative errors on the frequency are in the range $0.5\% < \frac{\Delta f}{f} < 1.7\%$ in the mixing layer. Taking into account the small values of uncertainty, evolution of the percentage of the relative errors has been reported on Fig. 15(c).

A continuous decrease of this characteristic frequency is clearly visible. At the beginning, for low x values corresponding to the splitter plate wake, values as high as 350–400 Hz are measured, then downstream, a rapid decrease occurs. In the self-similar region corresponding to values of x higher than about 80 mm, the main frequency continues to decrease. This frequency reduction is due to the pairing phenomenon: structures grow and travel at constant velocity U_C; they pair off when they interact with each other. Thus there are fewer and fewer structures as the observation point progresses further downstream.

From these peak frequency values and using the noncavitating large eddy convective velocity and the vorticity thickness longitudinal evolution as given in [12,22], we can compute the Strouhal

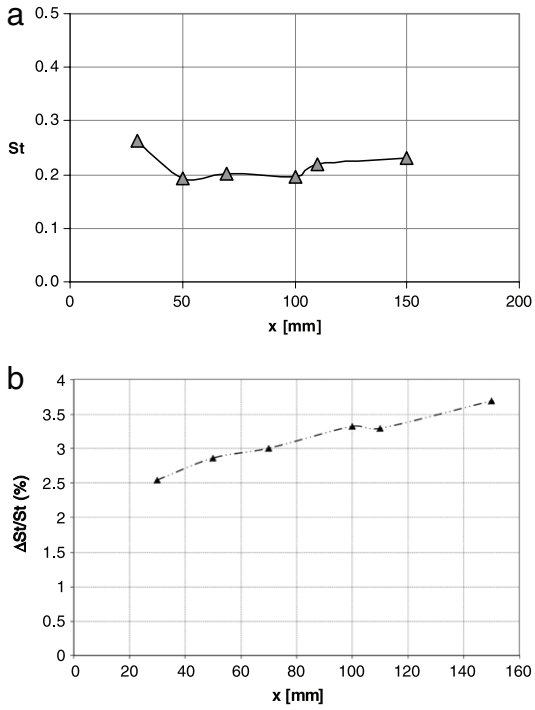

Fig. 16. (a) Longitudinal Strouhal number evolution (b) relative error evolution of Strouhal number, for the non-cavitating mixing layer.

number longitudinal evolution by using the following expression: $St = \frac{f\delta_\omega}{U_c}$. Results are plotted on Fig. 16(a) where the Strouhal number longitudinal evolution is displayed. Fig. 16(b) shows the evolution of the percentage of the relative error of the Strouhal number. Uncertainties are only due to the LDV resolution of the mean velocity value of about 2% and also the spectral resolution given previously. The maximum value is lower than 4% in the mixing layer.

It seems clear that, once the self-similar state is attained, the Strouhal number can be considered almost constant at a value close to 0.2.

In cavitating cases, the Strouhal number is determined using both the peak-to-peak cross-spectrum frequency as showed in Section 3.2 and the convective velocity. Fig. 17(a) shows the longitudinal evolution of the cross-spectrum amplitude peak frequency and the relative error is given on Fig. 17(b). These peak values are estimated with a maximum error of about 3%.

It is clear that this frequency evolves step by step in the longitudinal direction. We can observe a discrete reduction process corresponding to the growth of the mixing layer. At each step a strong brutal decrease is observed which may correspond to a kind of pairing process. It seems that, almost from a statistical point of view, the majority of the pairing events occur at well-determined longitudinal locations. Values of $x \approx 139$ and 204 mm are extracted for the $cav1$ case while for the $cav2$ case, values close to $x \approx 75$, 128 and 172 mm are found. Finally, for the $cav3$ flow, values of $x \approx 75$, 128 and 182 mm are observed. If we abstract all these data it seems that the cavitating mixing layer mainly experiences the pairing process at the end of the wake zone ($x \approx 75$ mm) and at two distinct and fairly well defined positions ($x \approx 130$ and 180–200 mm) in the self-similar zone. Cavitation seems to trigger the pairing process in a less random way than in the single phase mixing layer configuration where the peak frequency longitudinal evolution (see Fig. 15(b)) is more continuous corresponding to a quasi-randomly triggered pairing process mastered by the mixing layer thickness longitudinal evolution. Actually, despite the low repeatability of each event due to the high Reynolds number, we were able to sketch the pairing process as presented in Fig. 6. These schematic pictures show that neighbouring pairs of vortices roll around each other in the mixing layer leading to a vortex pairing phenomenon. Fig. 17(c) shows the longitudinal Strouhal number evolution for the three cavitating cases ($\sigma = 0.012$; 0.102 and 0.167). Errors bars are also plotted to put in evidence the precision of about 10% concerning the Strouhal determination in cavitating case using cross-correlation method. It is clear that these results are very scattered with Strouhal numbers ranging from 0.1 to 0.25 approximately. However, it can be easily argued that, as for convective velocities, no clear longitudinal trend can be found. Then, a global average value of about 0.15 can be extracted from the entire database corresponding to the three studied cases. It seems that cavitation has an effect on the Strouhal number value by decreasing it from 0.2 in non-cavitating cases to 0.15 in cavitating ones. However, the cavitation level does not seem to drastically affect the average Strouhal number value. At this stage, it is difficult to conclude as to whether the observed difference between the shedding process in single phase and two-phase flow is due to experimental uncertainties or to a real physical effect of the vapour in the vortex core. Actually, vortex pairing has been described by Winant and Browand [13] as the dominant mode of interaction and the principal mechanism for growth ("neighbouring pairs of vortices rotate around each other and amalgamate into a larger one"). Taking into account the large Reynolds number value in the present case $\left(R = \frac{\Delta U \rho \delta_\omega}{\mu} \approx 2.5 \times 10^5\right)$ it seems difficult to highlight the interacting process of vortices using the conditional method based on LDV technique. Nevertheless, in cavitating cases, the presence of the vapour phase seems to provoke sufficient irregularities to enhance pairing as observed on the Strouhal evolution along the mixing layer. Furthermore, we must not lose sight of the fact that the cavitation process is associated with growths and collapses linked with the pressure fluctuations. Vortex pairing affects the pressure inside the vortex cores and consequently the void ratio. Then cavitation process can be seen as a kind of "tracer" of the pairing process.

4. Conclusion

Using high-speed visualizations, cavitating vortices were examined in the two-dimensional cavitating mixing layer. A specific image processing based on the grey level transversal profiles of the frames and a spatio-temporal correlation method has been performed in order to highlight the dynamics of the large scale structures. To show the effects of the vapour phase on the dynamics of the mixing layer, systematic comparisons between the single and two-phase flows have been performed. The originality of the present work consisted in the achievement of different spatio-temporal approaches to characterize the shedding process, convective velocity, spatio-temporal diagram and coherence of the cavitating vortices coupled with a determination of the vapour thickness expansion. The main result is that no major change can be observed in the thickness evolution of the mixing layer due to the presence of the vapour phase. This result consists in a quasi-linear longitudinal evolution of the vapour thickness making that the selfsimilarity is preserved when cavitation number decreases inducing a similar development of Kelvin–Helmholtz eddies as what is observed in single phase flow. The determination of the convective velocity using spatio-temporal diagram and cross-correlation method leads to an estimation which is in a quite good agreement with the theoretical value. The velocity seems unaffected by the presence of the vapour phase in the kernel of the vortices. However, visualizations allow us to characterize and localize the pairing process of Kelvin–Helmholtz vortices. It seems that in cavitating cases, the pairing process is triggered in a less

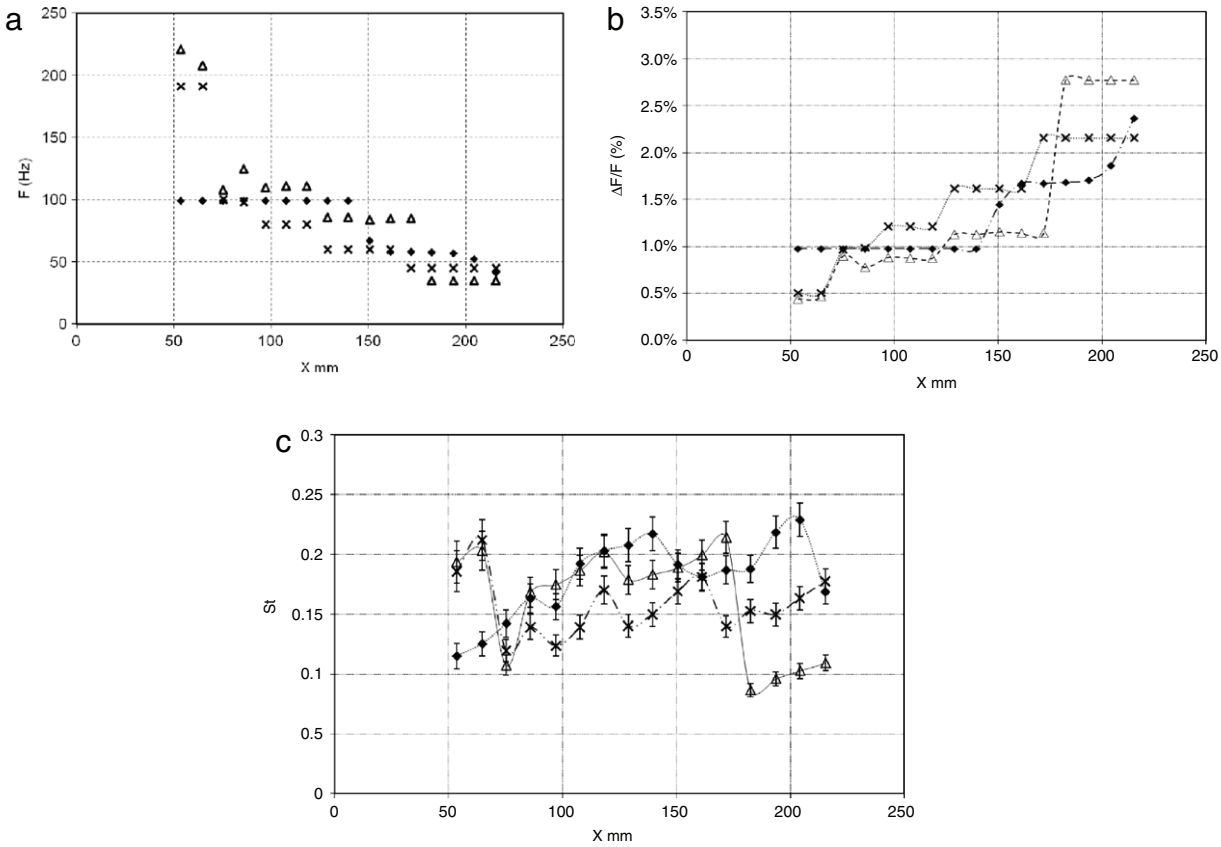

Fig. 17. (a) Frequency evolution, (b) Relative error of the frequency evolution, (c) Strouhal number evolution in the mixing layer for cavitating mixing layers, ♦: $\sigma = 0.167$ ($cav1$), ×: $\sigma = 0.102$ ($cav2$), △: $\sigma = 0.012$ ($cav3$).

random way than in the single phase flow. This effect is perhaps linked to a change in the acoustical impedance of the global flow due to the very great speed of sound gradient between the core and the boundaries of the turbulent cavitating mixing layer.

Acknowledgements

The authors wish to express their gratitude to the French Space Agency (CNES) and the rocket engine division of SNECMA for their continuous support. The technical support was given by F. Bonnel (Grenoble-INP, France).

References

[1] W. Hassan, Développement d'un système tomographique pour l'étude expérimentale du volume de vapeur présent au sein des turbopompes des machines spatiales, Thèse de doctorat INPG, Grenoble 2005.
[2] K. Kamijo, T. Shimura, M. Watanabe, An experimental investigation of cavitating inducer instability, ASME Paper 77-WA/FW-14, 1977.
[3] B. Stutz, J.-L. Reboud, Two-phase flow structure of sheet cavitation, Phys. Fluids 9 (1997) 3678.
[4] B. Stutz, J.L. Reboud, Experiments one unsteady cavitation, Exp. Fluids 22 (1997) 191.
[5] B. Stutz, J.-L. Reboud, Measurements within unsteady cavitation, Exp. Fluids 29 (2000) 545.
[6] S. Barre, J. Rolland, G. Boitel, E. Goncalves, R. Fortes-Patella, Experiments and modeling of cavitating flows in Venturi: attached sheet cavitation, Eur. J. Mech. B/Fluids 28 (2009) 444.
[7] T.M. Pham, F. Larrarte, D.H. Fruman, Investigation of unsteady sheet cavitation and cloud cavitation mechanisms, J. Fluids Eng. 121 (1999) 289.
[8] O. Coutier, B. Stutz, A. Vabre, S. Legoupil, Analysis of cavitating flow structure by experimental and numerical investigations, J. Fluid Mech. 578 (2007) 171.
[9] T.J. O'Hern, An experimental investigation of turbulent shear flow cavitation, J. Fluid Mech. 215 (1990) 365.
[10] C.O. Iyer, S.L. Ceccio, The influence of developed cavitation on the flow of a turbulent shear layer, Phys. Fluids 14 (2002) 3414.
[11] K.R. Laberteaux, S.L. Ceccio, Partial cavity flows. Part 1. Cavities forming on models without spanwise variation, J. Fluid Mech. 431 (2001) 1.
[12] V. Aeschlimann, S. Barre, S. Legoupil, X-ray attenuation measurements in a cavitating mixing layer for instantaneous two-dimensional void ratio determination, Phys. Fluids 23 (2011) 055101.
[13] C.D. Winant, F.K. Browand, Vortex pairing: the mechanism of turbulent mixing-layer at moderate Reynolds number, J. Fluid Mech. 63 (1974) 237.
[14] G. Brown, A. Roshko, On density effects and large structure in turbulent mixing layers, J. Fluid Mech. 64 (1974) 775.
[15] D. Papamoschou, A. Roshko, The compressible turbulent shear layer: an experimental study, J. Fluid Mech. 197 (1988) 453.
[16] S.L. Ceccio, C.E. Brennen, Observation of the dynamics and acoustics of travelling bubble cavitation, J. Fluid Mech. 233 (1991) 633.
[17] K.R. Labertaux, S.L. Ceccio, V.J. Mastrocola, J.L. Lowrance, High speed digital imaging of cavitating vortices, Exp. Fluids 24 (1998) 489.
[18] Y. Saito, K. Sato, Growth process to cloud-like cavitation on separated shear layer, in: 4th ASME-JSME Joint Fluids Engineering Conference, Honolulu, Hawaii, USA, July 6–10, 2003.
[19] Y. Saito, K. Sato, Bubble colapse propagation and pressure wave at periodic cloud cavitation, in: 6th International Conference on Multiphase Flow, ICMF 2007, Leipzig, Germany, July 9–13, 2007.
[20] J.E. Sargison, G.J. Walter, R. Rossi, Design and calibration of a wind tunnel with a two dimensional contraction, in: 15th Australian Fluid Mechanics Conference, December 2004, Sydney, Australia, 2004.
[21] R.E.A. Arndt, Cavitation in Vortical Flows, Annu. Rev. Fluid Mech. 34 (2002) 145.
[22] V. Aeschlimann, S. Barre, H. Djeridi, Velocity field analysis in an experimental cavitating mixing layer, Phys. Fluids 23 (2011) 055105.